BILINGUAL PUBLISHING GROUP

Journal of Building Material Science
https://journals.bilpubgroup.com/index.php/jbms

ARTICLE

Influence of Aragonite-Derived Bio-Calcium on Hydration Products and Microstructure of Cement Paste

Chakkarphan Sangsuwan [1], ***Worachai Ponloa*** [2*]

[1] *Department of Civil Engineering, Faculty of Engineering, Rajamangala University of Technology Phra Nakhon, Bangkok 10300, Thailand*

[2] *Department of Civil Engineering, Faculty of Engineering, Bangkokthonburi University, Bangkok 10170, Thailand*

ABSTRACT

Aragonite-derived bio-calcium originates from food industry waste and has potential for partial replacement of ordinary Portland cement (OPC) in cementitious systems. The objective was to study the effect of partial replacement of OPC with cuttlebone powder (CBP) on hydration products and microstructure. The six mixture groups used CBP contents of 0%, 10%, 20%, 30%, 40%, and 50% to partially replace OPC by weight at a constant water-to-binder ratio of 0.5. The specimens were cured under submerged water conditions for 28 days. X-ray diffraction (XRD), Fourier-transform infrared spectroscopy (FTIR), thermogravimetric/derivative thermogravimetric (TG/DTG), scanning electron microscopy (SEM), and energy-dispersive X-ray spectroscopy (EDS) analyses were conducted to evaluate hydration-related characteristics and microstructure evolution. The results showed that calcium hydroxide (CH)-associated weight loss decreased from 7.41% in the control specimen to 3.98% in CBP40, whereas carbonate-associated weight loss increased from 2.80% to 15.06% in CBP50. Carbonate decomposition midpoint increased from 688.25 °C to 767.41 °C after CBP incorporation. XRD and FTIR showed broader diffraction profiles and carbonate-related absorption bands. SEM revealed granular morphology in CBP10–CBP30, whereas CBP40 and CBP50 exhibited heterogeneous and agglomerated morphology. EDS showed that the Ca atomic percentage increased from approximately 66% to 82%, whereas the Si atomic percentage decreased from approximately 31% to 16%. CBP modified hydration products and microstructure, particularly at replacement levels of 20–30%. Higher replacement levels promoted stronger

*CORRESPONDING AUTHOR:
Worachai Ponloa, Department of Civil Engineering, Faculty of Engineering, Bangkokthonburi University, Bangkok 10170, Thailand;
Email: worachai.pon@bkkthon.ac.th

ARTICLE INFO
Received: 14 June 2026 | Revised: 30 June 2026 | Accepted: 20 July 2026 | Published Online: 20 August 2026
DOI: https://doi.org/10.30564/jbms.v8i3.13648

CITATION
Sangsuwan, C., Ponloa, W., 2026. Influence of Aragonite-Derived Bio-Calcium on Hydration Products and Microstructure of Cement Paste. Journal of Building Material Science. 8(3): 143–158. DOI: https://doi.org/10.30564/jbms.v8i3.13648

COPYRIGHT
Copyright © 2026 by the author(s). Published by Bilingual Publishing Group. This is an open access article under the Creative Commons Attribution-NonCommercial 4.0 International (CC BY-NC 4.0) License (https://creativecommons.org/licenses/by-nc/4.0/).

carbonate-associated characteristics and more heterogeneous morphology. Further investigation is required to clarify the mechanism before CBP can be fully evaluated as a partial replacement for OPC.

Keywords: Bio-Calcium; Cuttlebone Powder; Hydration Products; SEM–EDS; Cement Paste

1. Introduction

Global carbon dioxide (CO_2) emissions from industrial processes remain a major environmental issue [1]. The cement industry contributes considerably to these emissions because cement production requires high energy consumption and clinker manufacturing at elevated temperatures [2–4]. A large amount of CO_2 generated during cement production originates from limestone calcination during clinker formation [5]. During this process, calcium carbonate ($CaCO_3$) decomposes into calcium oxide (CaO) and releases CO_2 [5]. Fuel combustion used to maintain kiln operation also increases total emissions from cement manufacturing [6]. Therefore, reducing clinker content in cementitious systems has become an important strategy for decreasing CO_2 emissions associated with cement production [7,8]. As a result, supplementary and alternative mineral materials have attracted attention as potential components for low-carbon cement-based materials [7].

Supplementary cementitious materials (SCMs) change hydration reactions and microstructural development in cementitious systems [9–11]. They also influence microstructural development during hydration [12–14]. These materials consume calcium hydroxide released during cement hydration and contribute to the formation of additional calcium silicate hydrate (C–S–H) and calcium aluminate hydrate phases [15,16]. The incorporation of SCMs also modifies hydration kinetics, reaction heat, and phase development during the early stage of hydration [17,18]. The formation of secondary hydration products can reduce pore connectivity and produce a denser cement matrix [19,20]. These changes can decrease ion transport and improve matrix integrity in hardened cement systems [19–21]. However, calcium leaching and progressive decalcification may gradually destabilize hydration products and increase pore development within the cement matrix [20–23]. Decalcification weakens the C–S–H structure and reduces microstructural stability under aggressive conditions [21–23]. Hydration products, pore structure, and calcium-rich materials interact throughout cement hydration. These interactions influence the performance of modified cementitious materials [24,25].

Cement hydration involves chemical reactions and ion transport within the cement matrix [26]. Nucleation creates active surfaces for hydration product precipitation and clinker dissolution. Early hydration proceeds more rapidly after nucleation [26]. Ion transport and water movement in the pore solution regulate hydrate formation during the early hydration stage [27]. Fine mineral materials modify hydration through surface interactions and changes in pore solution chemistry. Sulfate availability and particle-surface adsorption also influence hydration reactions during cement hydration [27,28]. Chemical reactions and transport processes modify hydration products and pore structure throughout cement hydration [26–28].

Hydration in blended cement systems depends on clinker hydration, dilution effects, filler action, and pozzolanic reactions [29]. Fine mineral particles provide nucleation sites for hydrate precipitation. Low replacement levels promote early hydration [30]. Higher replacement levels reduce clinker dissolution. Fewer reactive cement phases remain available for hydration, and hydration heat release decreases [30]. Reactive aluminosilicate phases consume calcium hydroxide released during cement hydration. Secondary calcium silicate hydrate (C–S–H) and calcium aluminate hydrate phases form during later hydration periods [31]. Dissolution–precipitation reactions within the pore solution regulate hydrate phase assemblage and matrix formation in cementitious materials [32]. Surface interactions between cement grains and fine mineral particles modify pore structure and hydration behavior [33]. Hydration reactions continuously modify hydration products and pore structure throughout cement hydration [34].

C–S–H serves as the primary binding phase in cementitious systems, and its formation depends on the Ca/Si ratio and hydration conditions [35]. The Ca/Si ratio controls gel structure, phase assemblage, and hardened matrix properties [35,36]. A suitable Ca/Si ratio produces a denser C–S–H network. Matrix continuity improves at the microscale under these conditions [36]. Calcium concentration within the pore solution regulates ion mobility,

water transport, and local hydration reactions during cement hydration [37]. Supplementary cementitious materials modify hydration through dilution effects, secondary hydration reactions, and dissolution–precipitation processes in the pore solution [38]. Blended carbonate–clay systems generate C–S–H, ettringite, portlandite, and carboaluminate-related phases [39,40]. System composition and hydration conditions determine the formation of these hydration products [39,40]. SCMs reduce clinker consumption and modify hydration behavior in cementitious systems [41]. High $CaCO_3$ content allows calcium-rich shell-derived materials to participate in hydration reactions. Hydration products formed from these reactions modify the microstructure of cement paste [42,43].

Cuttlebone powder (CBP) is a marine-derived calcium carbonate material composed predominantly of aragonite [43,44]. Previous studies have used cuttlebone-derived materials in mortar and concrete as filler materials and supplementary additives [45,46]. Aragonite differs from calcite in crystal structure and hydration-related behavior in cementitious systems [47,48]. Aragonite and calcite differ in hydration behavior in cement-based materials [48–50]. However, the influence of aragonite-derived CBP on hydration-related characteristics and microstructure evolution of cement paste remains unclear.

Fine shell particles may provide nucleation sites for hydrate precipitation and modify dissolution–precipitation processes during hydration [51]. In carbonate-bearing systems, hydration behavior also depends on the crystal structure of calcium carbonate polymorphs, particularly calcite and aragonite, which exhibit different nucleation characteristics and surface interactions during hydration [52]. These polymorph-related interactions can affect hydration kinetics and carbonate-associated phase formation within the cement matrix [52]. The development of hydration products is closely related to the formation of C–S–H, whose structure and morphology depend strongly on the Ca/Si ratio and local hydration conditions [53–55]. Changes in hydration conditions can alter pore structure and matrix continuity in hardened cement systems [54–56].

Previous studies on cuttlebone powder mainly reported strength development and mechanical performance of cementitious materials. In contrast, fewer studies have examined its influence on hydration products and microstructure development of cement paste. The effects of CBP incorporation on CH-related behavior, carbonate-associated phases, hydration product morphology, and elemental characteristics have received limited attention. Moreover, the influence of high CBP replacement levels on matrix continuity and microstructural heterogeneity has not been thoroughly investigated.

Therefore, this study investigated the influence of aragonite-derived bio-calcium on hydration products, thermal behavior, and microstructure development of cement paste incorporating CBP. The study evaluated CH-related behavior, carbonate-associated phases, hydration product morphology, and elemental characteristics to explain the hydration behavior of CBP. XRD, FTIR, TGA/DTG, SEM, and EDS analyses supported the interpretation of these characteristics.

2. Materials and Methods

2.1. Materials

OPC served as the base binder in all mixtures and satisfied ASTM C150-24 Type I [57]. CBP consisted mainly of aragonite. CBP partially replaced OPC in the cement paste mixtures. CBP preparation involved cleaning to remove organic matter, drying, and grinding into powder. The CBP powder passed through a No. 100 sieve according to ASTM E11-24 [58] to obtain a controlled particle size for uniform mixing, as shown in **Figure 1**. The sample mixtures used deionized water at a constant water-to-binder (w/b) ratio of 0.5. CBP replaced 0%, 10%, 20%, 30%, 40%, and 50% of OPC by weight of cement. The mixture without CBP served as the control. **Table 1** summarizes the mix proportions.

2.2. Methods

2.2.1. Chemical Composition Analysis (XRF)

XRF determined the chemical compositions of OPC and CBP using a PANalytical SuperQ system under controlled conditions. The analysis quantified the major and minor oxide contents of both materials. OPC consisted mainly of CaO, SiO_2, Al_2O_3, and Fe_2O_3, together with smaller amounts of MgO, Na_2O, and K_2O. In contrast, CBP contained predominantly CaO. These results provided

the chemical basis for comparing the compositions of OPC and CBP before paste preparation.

(**a**) (**b**)

Figure 1. Materials: (**a**) CBP; (**b**) OPC.

Table 1. Mix proportions.

Specimen	OPC (% by Weight)	CBP (% by Weight)	Water-to-Binder Ratio
Control	100	0	0.5
CBP10	90	10	0.5
CBP20	80	20	0.5
CBP30	70	30	0.5
CBP40	60	40	0.5
CBP50	50	50	0.5

2.2.2. Specimen Preparation

OPC and CBP formed the binder system. Dry materials were mixed before adding deionized water. Mixing followed ASTM C305-20 [59] and produced a paste. The fresh paste was filled into 50 × 50 × 50 mm cube molds according to ASTM C109-20 [60]. The specimens were demolded after 24 h and cured in water at 25 ± 2 °C for 28 days according to ASTM C511-21 [61]. The mix proportions are listed in **Table 1**. **Figure 2** shows the specimen preparation procedure.

(**a**) (**b**)

Figure 2. Cement paste specimen preparation: (**a**) paste mixing; (**b**) specimen casting.

2.2.3. Phase Analysis by X-Ray Diffraction (XRD)

XRD determined the crystalline phases of the cement paste specimens. Measurements were performed using a Bruker D8 Advance diffractometer equipped with Cu Kα radiation (λ = 1.5406 Å) at 40 kV and 40 mA. The scan covered a 20 range of 5–60° with a step size of 0.02° and a scanning rate of 1°/min. Phase identification included CH, ettringite, residual clinker phases, and aragonite associated with CBP.

2.2.4. Fourier-Transform Infrared Spectroscopy (FTIR)

FTIR characterized the functional groups associated with cement hydration. A Bruker Tensor II FTIR spectrometer recorded spectra over the 400–4,000 cm^{-1} range using the KBr pellet technique. The spectra identified silicate bands related to C–S–H, carbonate absorption bands associated with residual or transformed $CaCO_3$, and bands corresponding to OH and SO_4^{2-} groups. These results provided molecular-scale information for evaluating hydration products and the influence of CBP on the cement system.

2.2.5. Thermogravimetric Analysis (TGA)

TGA evaluated the thermal behavior of the cement paste specimens using a TA Instruments Q50. Approximately 20–25 mg of each sample was heated from room temperature to 1,000 °C under a nitrogen atmosphere at a heating rate of 10 °C/min. The mass-loss profile identified C–S–H dehydration, CH decomposition, and $CaCO_3$ decarbonation. These results provided quantitative information for evaluating hydration products and carbonation reactions associated with CBP.

2.2.6. Scanning Electron Microscopy (SEM)

SEM characterized the microstructure of the cement paste specimens. After 28 days of curing, the specimens were fractured into small pieces and immersed in acetone for 24 h to stop hydration. The fractured surfaces were coated with gold and examined using a JEOL JSM-IT500 scanning electron microscope. The analysis focused on hydration products, pore structure, surface morphology, and phase distribution within the cement matrix.

2.2.7. Energy-Dispersive X-Ray Spectroscopy (EDS)

Energy-dispersive X-ray spectroscopy (EDS) analyzed the elemental composition of hydration products in the cement paste specimens. The EDS analysis was conducted together with SEM observation using a JEOL JSM-IT500 system. The analysis examined the SEM observation regions. The EDS spectra determined the Ca/Si ratio and elemental composition of the selected regions. The spectra also detected Na, Mg, and Sr associated with CBP.

3. Results

3.1. Chemical Composition of Raw Materials (XRF)

OPC and CBP exhibited markedly different chemical compositions based on XRF analysis, as shown in **Table 2**. CaO dominated the composition of CBP and reached 95.07%, exceeding the corresponding value of OPC (78.18%). OPC contained substantially higher amounts of SiO_2, Al_2O_3, and Fe_2O_3. The SiO_2 content reached 11.29% in OPC but remained at only 0.03% in CBP. XRF also detected minor oxides, including Na_2O, MgO, K_2O, SrO, ClO_2, and P_2O_5, in CBP. CBP contained predominantly calcium-bearing oxides. OPC contained the major silicate-bearing components in the cement system.

Table 2. Chemical composition of OPC and CBP.

Material	Oxide Composition, (%)											
	Al_2O_3	SiO_2	CaO	Fe_2O_3	Na_2O	MgO	K_2O	SO_3	SrO	TiO_2	ClO_2	P_2O_5
OPC	2.83	11.29	78.18	3.29	0.24	1.31	0.41	1.82	-	0.32	0.24	0.06
CBP	0.02	0.03	95.07	-	1.52	0.16	0.19	0.42	0.63	-	1.62	0.22

3.2. Phase Composition and Hydration Products (XRD)

CH-related reflections appeared at approximately 18°, 34°, and 47° in both the control and CBP-modified cement paste specimens. Low-angle reflections appeared between approximately 7° and 12° and between 27° and 31°. A broad diffraction region extended from approximately 27°–34°. Low-crystallinity C–S–H-related phases were associated with the broad diffraction region, as shown in **Figure 3**.

The diffraction peak near 18° remained the most intense CH-related reflection throughout all CBP replacement levels. The control specimen exhibited sharp diffraction peaks with high relative intensity. CBP replacement produced broader diffraction profiles and reduced the relative intensity of the CH-related reflections. Peak broadening increased from CBP30 onward. CBP40 and CBP50 produced the broadest diffraction profiles and the lowest relative intensity in the CH-related region near 34°.

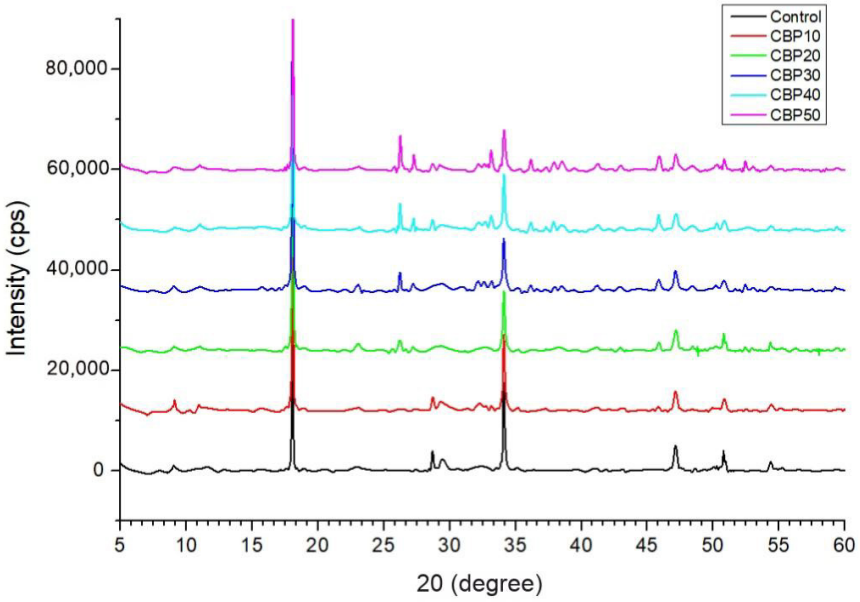

Figure 3. XRD patterns of the control and CBP-modified cement paste specimens.

The control specimen showed low diffraction intensity between approximately 7° and 12°. CBP incorporation increased the relative intensity between approximately 7° and 12°. CBP30, CBP40, and CBP50 produced the highest relative intensity in this range. Low-angle reflections appeared between approximately 27° and 31°. Relatively weak reflections were observed in the control specimen, whereas the CBP-modified specimens exhibited more distinguishable reflections after CBP incorporation. These low-angle reflections may be associated with AFt- or ettringite-related hydration phases.

A broad and diffuse diffraction region was observed between approximately 27° and 34°. A relatively sharper diffraction profile was observed in the control specimen, whereas broader and more diffuse profiles developed after CBP incorporation. In addition, the relative intensity gradually decreased with increasing CBP replacement. The broad diffraction profile observed in this region may be related to low-crystallinity C–S–H-related phases.

3.3. Functional Groups and Molecular Characteristics (FTIR)

The FTIR spectra of the control and CBP-modified cement paste specimens are presented in **Figure 4**. A broad absorption band appeared at approximately 3,430 cm^{-1} in all mixtures, while additional absorption bands were observed at approximately 1,640, 1,450, 1,030, and 870 cm^{-1}. These absorption bands were associated with hydration-related, CO_3^{2-}-related, and Si–O-related vibration regions within the cement paste system. The control specimen exhibited higher transmittance and narrower absorption profiles in these regions, whereas the CBP-modified

specimens showed lower transmittance, deeper absorption bands, and broader spectral profiles after CBP incorporation. Broader and more pronounced absorption bands appeared at approximately 1,450 and 870 cm^{-1} with increasing CBP replacement. The most pronounced absorption bands appeared in CBP40 and CBP50.

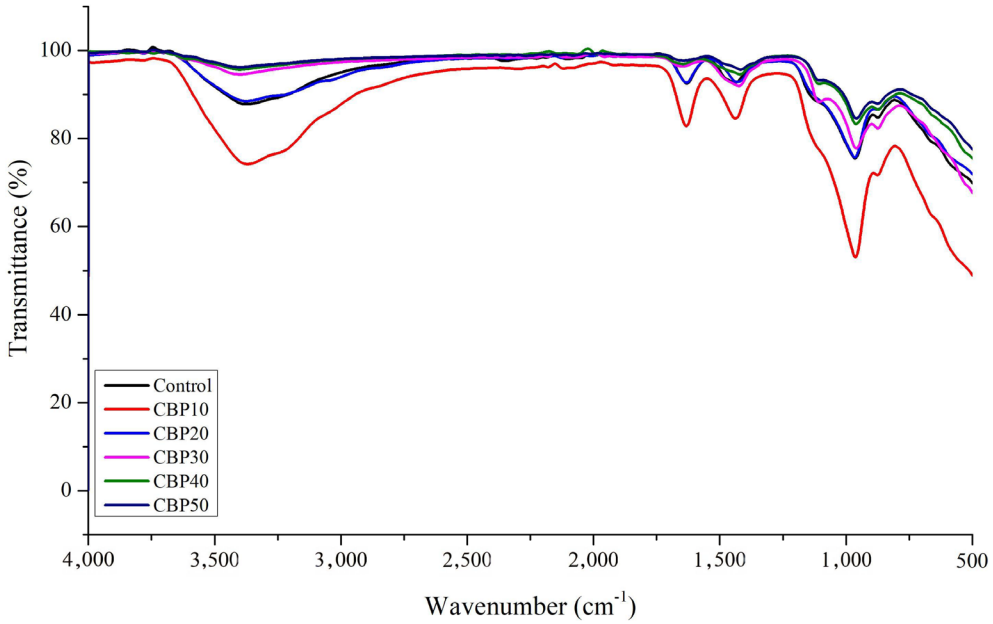

Figure 4. FTIR spectra of control and CBP-modified cement paste specimens.

FTIR spectra showed a broad absorption band at approximately 3,430 cm^{-1} in all mixtures. An absorption band appeared at approximately 1,640 cm^{-1}. The band at 3,430 cm^{-1} corresponded to the O–H stretching vibration. The band at 1,640 cm^{-1} represented the H–O–H bending vibration. The control specimen showed higher transmittance and narrower absorption profiles. CBP-modified specimens exhibited lower transmittance and deeper absorption bands. Band broadening occurred at approximately 3,430 cm^{-1} after CBP incorporation. CBP20, CBP40, and CBP50 exhibited the greatest band broadening.

Carbonate-related absorption bands appeared at approximately 1,450 and 870 cm^{-1}. The bands corresponded to the CO_3^{2-} vibration regions of the cement paste system. The control specimen showed higher transmittance and narrower absorption profiles. CBP-modified specimens showed lower transmittance and deeper absorption bands. The absorption bands at approximately 1,450 and 870 cm^{-1} became broader. CBP40 and CBP50 exhibited the greatest band broadening. The results reflected the carbonate-rich nature of CBP.

An absorption band appeared at approximately 1,030 cm^{-1}. The band corresponded to the Si–O-related vibration region of the cement paste system. The control specimen showed a narrower absorption profile. CBP-modified specimens showed broader absorption profiles and lower transmittance. The absorption band at approximately 1,030 cm^{-1} became more visible. The absorption band was most visible in CBP30, CBP40, and CBP50.

3.4. Thermal Decomposition Behavior (TGA)

The TG and DTG curves are shown in **Figure 5**. Three decomposition regions appeared in the control specimen and the CBP mixtures. The first region corresponded to dehydration-related weight loss. CH decomposition appeared in the second region, whereas carbonate decomposition appeared at higher temperatures. Quantitative results are summarized in **Table 3**. The control specimen showed a CH-associated weight loss of 7.41%. Lower values between 3.98% and 6.30% were observed in the CBP mixtures. In contrast, carbonate-associated weight loss increased from 2.80% in the control specimen to 15.06% in CBP50. The carbonate decomposition midpoint increased from 688.25 °C in the control specimen to 767.41 °C in CBP50. The DTG curves of the CBP mixtures showed

broader peaks in the carbonate decomposition region com- pared with the control specimen.

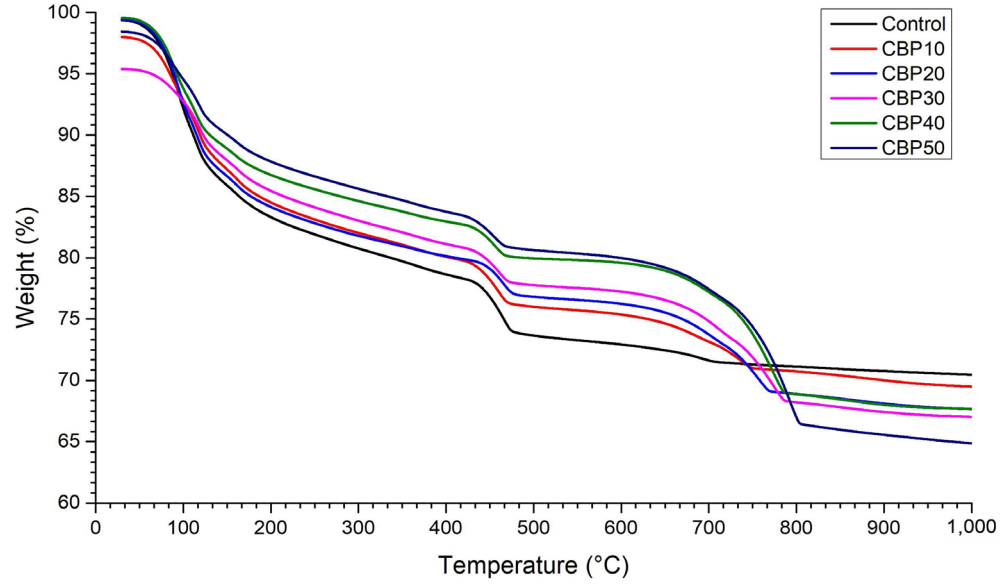

(**a**)

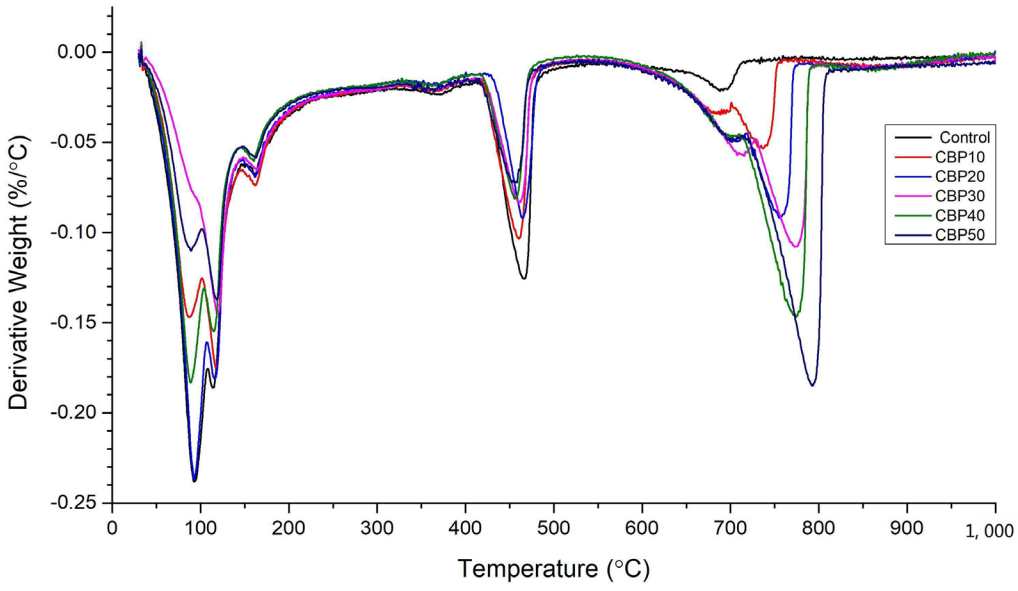

(**b**)

Figure 5. (**a**) TG curves and (**b**) DTG curves of control and CBP-modified cement paste specimens.

Table 3. Weight-loss characteristics of cement paste specimens obtained from TG/DTG analysis.

Specimen	Low-Temperature Weight Loss (%)	CH-Associated Weight Loss (%)	Carbonate-Associated Weight Loss (%)	Carbonate Decomposition Midpoint (°C)	Final Residue
Control	18.68	7.41	2.80	688.25	70.46
CBP10	16.15	6.30	6.01	718.63	69.50
CBP20	17.91	5.02	8.80	732.83	67.66
CBP30	13.49	4.42	10.44	745.48	67.02
CBP40	15.82	3.98	12.03	750.76	67.69
CBP50	13.13	5.33	15.06	767.41	64.87

The low-temperature decomposition region appeared below approximately 200 °C in **Figure 5**. Quantitative results are summarized in **Table 3**. Weight loss in this region ranged between 13.13% and 18.68%. The control specimen showed the highest low-temperature weight loss of 18.68%, whereas CBP30 and CBP50 showed lower values of 13.49% and 13.13%, respectively. The DTG curves in **Figure 5** showed variations in the low-temperature decomposition region among the mixtures. Several CBP mixtures showed broader DTG peaks compared with the control specimen.

The CH decomposition region appeared between approximately 430 °C and 500 °C in **Figure 5**. CH-associated weight loss decreased from 7.41% in the control specimen to 3.98% in CBP40. Lower decomposition peaks appeared in the DTG curves after CBP incorporation. The reduction in CH-associated weight loss corresponded to lower decomposition peaks in the CH region. CH-associated weight loss remained between 4.42% and 5.02% in CBP20–CBP30, whereas CBP50 showed a slight increase to 5.33% compared with CBP40.

The carbonate decomposition region appeared at higher temperatures in **Figure 5**. Carbonate-associated weight loss increased from 2.80% in the control specimen to 15.06% in CBP50. The control specimen showed the lowest carbonate-associated decomposition, whereas CBP50 showed the highest decomposition among the mixtures. The carbonate decomposition midpoint shifted from 688.25 °C in the control specimen to 767.41 °C in CBP50. Higher carbonate-associated weight loss corresponded to broader decomposition peaks in the DTG curves after CBP incorporation. Broader decomposition peaks appeared in the carbonate decomposition region of the CBP mixtures compared with the control specimen.

The TG and DTG results showed differences in thermal decomposition behavior after CBP incorporation, as shown in **Table 4**. Lower CH-associated decomposition was accompanied by higher carbonate-associated decomposition in the CBP mixtures. The increase in carbonate-associated weight loss corresponded to broader decomposition peaks and elevated midpoint temperatures in the carbonate decomposition region.

Table 4. Comparative thermal decomposition behavior of cement paste specimens.

Specimen	Low-Temperature Thermal Response	CH-Associated Decomposition Behavior	Carbonate-Associated Decomposition Behavior	Thermal Decomposition Behavior
Control	Highest low-temperature weight loss	Strong CH decomposition	Limited carbonate decomposition	CH-dominant decomposition
CBP10	Reduced low-temperature weight loss compared with control	Lower CH decomposition	Increased carbonate decomposition	Shift toward carbonate decomposition
CBP20	Thermal response comparable to control	Further reduction in CH decomposition	More pronounced carbonate decomposition	Increased carbonate-related decomposition
CBP30	Reduced low-temperature thermal response	Reduced CH decomposition	Carbonate decomposition became dominant	Carbonate-dominant decomposition
CBP40	Moderate low-temperature thermal response	Lowest CH decomposition among the mixtures	Strong carbonate decomposition	Strong carbonate-dominant decomposition
CBP50	Lowest low-temperature weight loss among the mixtures	Slight increase in CH decomposition compared with CBP40	Highest carbonate decomposition and decomposition midpoint	Maximum carbonate-related decomposition

3.5. Microstructure and Morphology (SEM)

The incorporation of CBP modified the morphology of the cement matrix. Granular morphology appeared after CBP incorporation. Crystalline features appeared less distinct in several CBP mixtures. Surface continuity and pore regions varied among the mixtures. Agglomerated morphology was more evident at high CBP contents, as presented in **Figure 6**.

Compared with the control specimen, the CBP mixtures exhibited differences in matrix morphology and surface continuity. Granular morphology became more apparent in CBP10–CBP30. Crystalline features appeared less distinct than in the control specimen. Visible pore regions were less evident in several CBP mixtures, particularly in CBP30, where the matrix retained a relatively more continuous morphology. CBP40 and CBP50 exhibited more heterogeneous and agglomerated morphology compared with CBP10–CBP30. Clustered granular regions and irregular surface continuity were more

noticeable at high CBP contents. Localized pore regions remained visible in several areas of the matrix, particularly in CBP50, where heterogeneous morphology appeared across several regions.

The SEM observations were consistent with the TG and DTG results. Reduced crystalline morphology in several CBP mixtures corresponded to lower CH-associated decomposition behavior. In contrast, agglomerated and heterogeneous morphology were more noticeable at high CBP contents, where higher carbonate-associated decomposition was also observed. The SEM observations reflected differences in matrix morphology after CBP incorporation, particularly in granular texture, surface continuity, and heterogeneous morphology at high CBP contents.

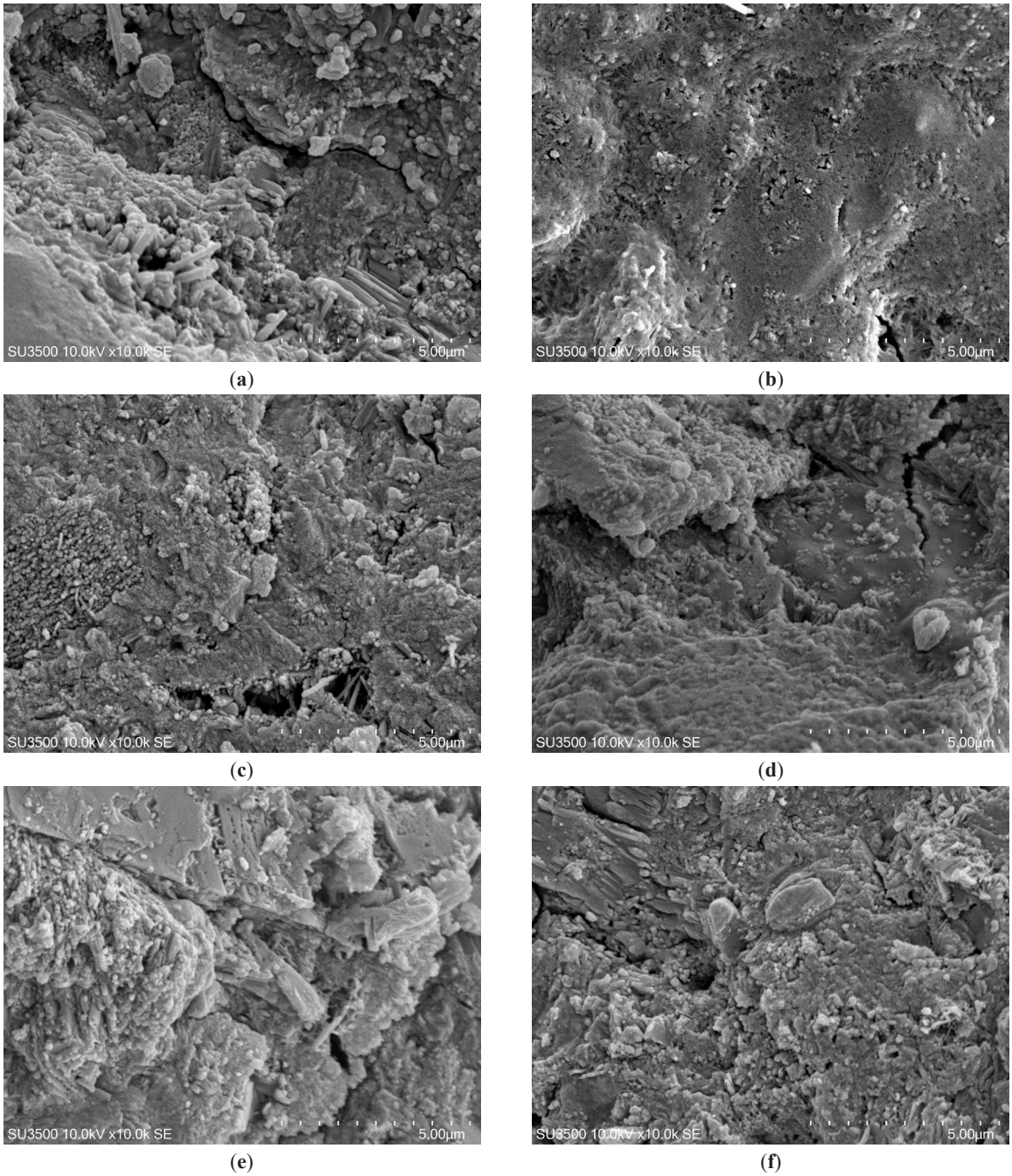

Figure 6. SEM micrographs: (**a**) Control; (**b**) CBP10; (**c**) CBP20; (**d**) CBP30; (**e**) CBP40; and (**f**) CBP50.

3.6. Elemental Characteristics of Hydration Products (EDS)

The EDS spectra showed differences in elemental characteristics after CBP incorporation, particularly in relative Ca and Si peak intensities, as shown in **Figure 7**. The CBP mixtures showed a gradual increase in Ca-related peak intensity, whereas the relative Si-related intensity became less noticeable at high CBP contents. Differences in morphology were also observed in the corresponding SEM observation regions across the mixtures.

The EDS results showed changes in Ca and Si atomic percentages after CBP incorporation. The Ca atomic percentage increased from approximately 66% in the control specimen to about 82% in CBP50, whereas the Si atomic percentage decreased from approximately 31% to 16%. Higher Ca atomic percentages were observed at high CBP contents, particularly in CBP40 and CBP50.

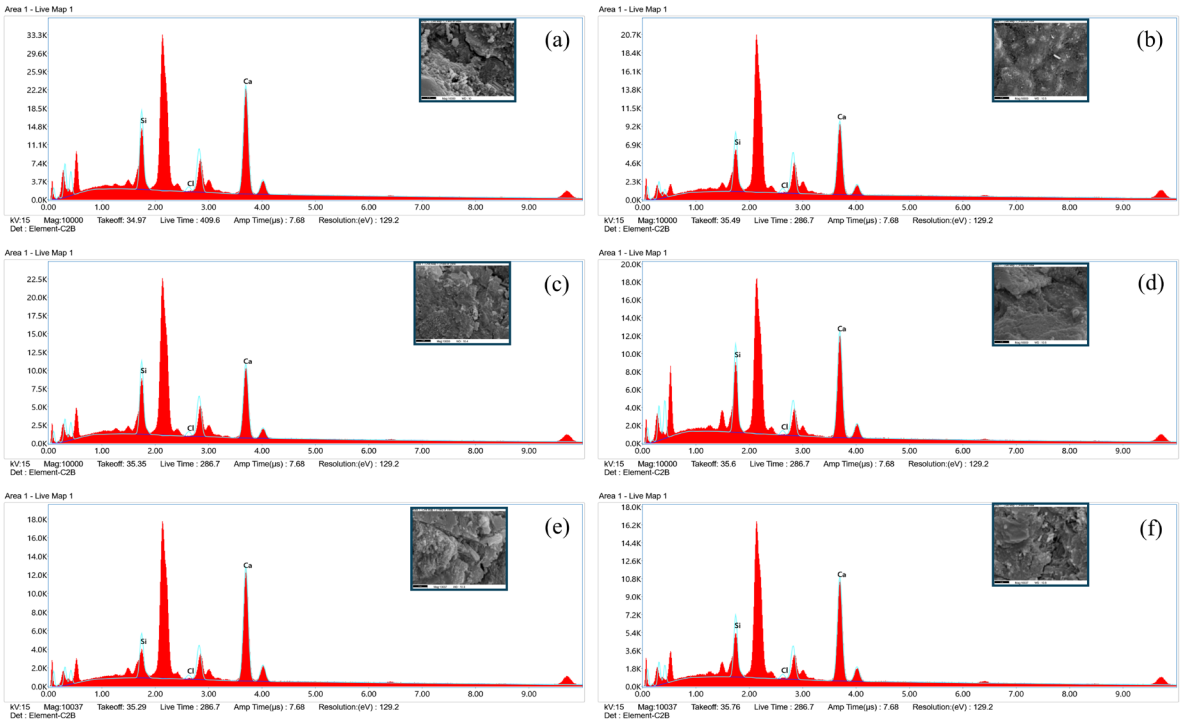

Figure 7. EDS spectra and corresponding SEM observation regions: (**a**) Control; (**b**) CBP10; (**c**) CBP20; (**d**) CBP30; (**e**) CBP40; and (**f**) CBP50.

The changes in Ca and Si atomic percentages corresponded to differences in morphology observed in the SEM observation regions. CBP40 and CBP50 exhibited higher Ca atomic percentages together with more heterogeneous and agglomerated morphology compared with the control specimen and the lower CBP mixtures. These morphological differences were more noticeable at high CBP contents. The results corresponded to the SEM and TG/DTG observations. Higher Ca atomic percentages at high CBP contents were observed together with more heterogeneous and agglomerated morphology. Lower relative Si atomic percentages also appeared across several CBP mixtures together with differences in matrix morphology.

4. Discussion

The XRD patterns showed broader diffraction profiles and lower relative intensity in the CH-related regions after CBP incorporation. **Figure 3** shows the corresponding diffraction patterns. The FTIR spectra showed broader carbonate-related absorption bands and lower transmittance behavior, particularly at high CBP contents. The corresponding FTIR spectra are shown in **Figure 4**. The TG/DTG results showed lower CH-associated decomposition and stronger carbonate-associated decomposition behavior after CBP incorporation. **Figure 5** shows the corresponding TG/DTG curves. More granular and agglomerated

morphology appeared after CBP incorporation, as observed in the SEM images shown in **Figure 6**. Higher Ca atomic percentages together with lower relative Si atomic percentages were also detected in the selected SEM observation regions of several CBP mixtures. The corresponding EDS spectra are shown in **Figure 7**.

Higher carbonate-associated decomposition appeared at high CBP contents, particularly in CBP40 and CBP50. Broader decomposition peaks together with higher decomposition midpoint temperatures were observed in the carbonate decomposition region of the TG/DTG curves shown in **Figure 5**. Broader carbonate-related absorption bands at approximately 1,450 and 870 cm^{-1} also appeared in the FTIR spectra shown in **Figure 4**. CBP40 and CBP50 exhibited more heterogeneous and agglomerated morphology than the lower CBP mixtures, as observed in **Figure 6**. Higher Ca atomic percentages were also detected in the selected SEM observation regions of these mixtures. **Figure 7** shows the corresponding EDS spectra.

CBP incorporation changed the matrix morphology. The control specimen showed more distinct crystalline morphology, visible pore regions, and discontinuous surface features. CBP10–CBP30 showed more granular morphology. Matrix continuity improved in several regions. These morphological differences are illustrated in **Figure 6**.

BP changed the hydration products and microstructure of cement paste after OPC replacement. The CH-related characteristics decreased, whereas the carbonate-related characteristics became more pronounced with increasing CBP content. Li et al. [49] reported similar changes in the hydration products and microstructure of cement paste containing both aragonite and calcite calcium carbonate. Their XRD, TG, and SEM analyses also identified carbonate-associated hydration products and different interactions between hydration products and calcium carbonate surfaces.

The hydration products and microstructural characteristics observed in this study are partly comparable with those reported by Jiang et al. [46], who reported similar hydration products and microstructural characteristics in aragonite-containing cementitious materials. Their study investigated hydration behavior and reaction products using hydration heat measurements, XRD, microstructural analysis, and multiscale characterization to explain the hydration mechanism. Hay et al. [52] investigated the hydration behavior of different calcium carbonate polymorphs using hydration kinetics together with XRD, TGA, and SEM analyses. Their results showed different hydration behavior among calcium carbonate polymorphs because of differences in crystal structure.

However, this study focused on characterizing hydration products and microstructural characteristics using XRD, FTIR, TG/DTG, SEM, and EDS. Further insight into the hydration mechanism and long-term performance of aragonite-derived bio-calcium will help explain its role in cement paste.

5. Conclusions

5.1. Hydration-Related Findings

Aragonite-derived bio-calcium modified the hydration-related behavior of cement paste after CBP incorporation. Lower CH-associated decomposition together with broader diffraction profiles and broader carbonate-related FTIR absorption bands appeared across the mixtures. These behaviors reflected differences in CH-related and carbonate-associated characteristics.

5.2. Microstructural Findings

The replacement of OPC with aragonite-derived CBP also changed the microstructure of the cement matrix. Differences in granular morphology, matrix continuity, and elemental characteristics appeared after CBP incorporation. The SEM observations showed changes in matrix morphology, whereas the EDS results showed higher Ca atomic percentages together with lower relative Si atomic percentages in several CBP mixtures. High CBP contents produced more heterogeneous and agglomerated morphology together with stronger carbonate-associated decomposition behavior. Broader carbonate-related FTIR absorption bands and higher Ca atomic percentages also appeared at high replacement levels. These differences became more pronounced in CBP40 and CBP50.

5.3. Study Summary and Future Work

The results show that CBP influences the formation of hydration products and microstructural development

in cement paste. Future work should clarify the hydration mechanism and assess long-term performance to better understand its potential in cementitious systems.

Author Contributions

Conceptualization, W.P.; methodology, W.P. and C.S.; investigation, C.S.; data curation, C.S.; visualization, C.S.; formal analysis, W.P.; writing—original draft, W.P.; writing—review and editing, W.P. and C.S.; supervision, W.P.; funding acquisition, W.P. Both authors have read and agreed to the published version of the manuscript.

Funding

This research received no external funding.

Institutional Review Board Statement

Not applicable.

Informed Consent Statement

Not applicable.

Data Availability Statement

The data presented in this study are available on request from the corresponding author.

Acknowledgments

The authors acknowledge Rajamangala University of Technology Phra Nakhon, Bangkok, Thailand, for laboratory facilities and technical support.

Conflicts of Interest

The authors declare no conflict of interest.

AI Use Statement

During the preparation of this manuscript, the authors used ChatGPT (OpenAI) for language editing and English grammar improvement. The authors subsequently reviewed and edited all outputs. The authors take full responsibility for the final content of the article.

References

[1] International Energy Agency (IEA), 2022. Global Energy Review: CO_2 Emissions in 2021: Global Emissions Rebound Sharply to Highest Ever Level. IEA: Cheltenham, UK.

[2] Liu, Z., Ciais, P., Deng, Z., et al., 2020. Carbon Monitor, a near-real-time daily dataset of global CO_2 emission from fossil fuel and cement production. Scientific Data. 7, 392. DOI: https://doi.org/10.1038/s41597-020-00708-7

[3] Costa, F.N., Ribeiro, D.V., 2020. Reduction in CO_2 emissions during production of cement, with partial replacement of traditional raw materials by civil construction waste (CCW). Journal of Cleaner Production. 276, 123302. DOI: https://doi.org/10.1016/j.jclepro.2020.123302

[4] Benhelal, E., Shamsaei, E., Rashid, M.I., 2021. Challenges against CO_2 abatement strategies in cement industry: A review. Journal of Environmental Sciences. 104, 84–101. DOI: https://doi.org/10.1016/j.jes.2020.11.020

[5] Danieli, S., Andrade Neto, J.S., Soares, E.G., et al., 2025. Shaping a sustainable path: Exploring opportunities and challenges in carbon capture and utilization in cement and concrete industry. Cement. 19, 100135. DOI: https://doi.org/10.1016/j.cement.2025.100135

[6] Proaño, L., Sarmiento, A.T., Figueredo, M., et al., 2020. Techno-economic evaluation of indirect carbonation for CO_2 emissions capture in cement industry: A system dynamics approach. Journal of Cleaner Production. 263, 121457. DOI: https://doi.org/10.1016/j.jclepro.2020.121457

[7] Supriya, Chaudhury, R., Sharma, U., et al., 2023. Low-CO_2 emission strategies to achieve net zero target in cement sector. Journal of Cleaner Production. 417, 137466. DOI: https://doi.org/10.1016/j.jclepro.2023.137466

[8] Dahmani, H., Ventura, A., Le Guen, L., et al., 2024. Life cycle assessment of cement: Are existing data and models relevant to assess the cement industry's climate change mitigation strategies? A literature review. Construction and Building Materials. 411, 134415. DOI: https://doi.org/10.1016/j.conbuildmat.2023.134415

[9] Cui, K., Zhao, D., Zhao, Y., et al., 2026. Development of CO_2-induced SCMs for calcium sulfoaluminate

cement: Towards enhancing hydration, compressive strength and later stage-ettringite stability. Cement and Concrete Research. 201, 108121. DOI: https://doi.org/10.1016/j.cemconres.2025.108121

[10] Gu, H., Yang, Z., Tao, Y., et al., 2025. The influence of SCMs on the pore structure evolution and carbonation of cement pastes under early carbonation. Construction and Building Materials. 465, 140194. DOI: https://doi.org/10.1016/j.conbuildmat.2025.140194

[11] Ng, S., Justnes, H., 2015. Influence of dispersing agents on the rheology and early heat of hydration of blended cements with high loading of calcined marl. Cement and Concrete Composites. 60, 123–134. DOI: https://doi.org/10.1016/j.cemconcomp.2015.04.007

[12] Kanagaraj, B., Anand, N., Samuel Raj, R., et al., 2023. Techno-socio-economic aspects of Portland cement, geopolymer, and limestone calcined clay cement (LC3) composite systems: A state-of-the-art review. Construction and Building Materials. 398, 132844. DOI: https://doi.org/10.1016/j.conbuildmat.2023.132484

[13] Han, S., Wi, S., Ji, K., et al., 2026. Transforming dredged sediment into reactive clay: Critical review of calcination, reactivity, and sustainable valorization as supplementary cementitious material. Applied Clay Science. 286, 108160. DOI: https://doi.org/10.1016/j.clay.2026.108160

[14] Park, C., Lee, J., 2024. Transforming biowaste into sustainable supplementary cementitious materials. Journal of Building Engineering. 98, 110976. DOI: https://doi.org/10.1016/j.jobe.2024.110976

[15] Jia, R., Ran, B., Lv, T., et al., 2025. Synergistic effect of waste concrete powder and traditional SCMs in preparing clinker-free cement: Hydration and microstructure evolution. Construction and Building Materials. 491, 142798. DOI: https://doi.org/10.1016/j.conbuildmat.2025.142798

[16] Xu, L., Wang, J., Hu, X., et al., 2024. Physical performance, durability, and carbon emissions of recycled cement concrete and fully recycled concrete. Construction and Building Materials. 447, 138128. DOI: https://doi.org/10.1016/j.conbuildmat.2024.138128

[17] Islam, M.S., Paul, S.C., Mohr, B.J., 2026. Hydration heat comparison of Portland cement blends with commonly available supplementary cementitious materials (SCMs) by isothermal calorimetry. Next Sustainability. 7, 100258. DOI: https://doi.org/10.1016/j.nxsust.2026.100258

[18] Li, Y., Liu, X., Zhu, Y., et al., 2026. Advancement of early strength of supplementary cementitious materials: A review. Journal of Building Engineering. 119, 115172. DOI: https://doi.org/10.1016/j.jobe.2025.115172

[19] Barnes, B.D., Diamond, S., Dolch, W.L., 1979. Micromorphology of the interfacial zone around aggregates in Portland cement mortar. Journal of the American Ceramic Society. 62(1–2), 21–24. DOI: https://doi.org/10.1111/j.1151-2916.1979.tb18797.x

[20] Xu, L., Wang, J., Huang, R., et al., 2025. Effects of accelerated carbonation on the chemical and microstructural evolution of recycled cement SCMs blended cement pastes. Cement and Concrete Composites. 164, 106259. DOI: https://doi.org/10.1016/j.cemconcomp.2025.106259

[21] Mahmoudi, S., O'Driscoll, J.H., O'Shea, M., et al., 2026. Review of deterioration mechanisms and durability performance mapping of sustainable SCM concrete in wastewater environments. Journal of Building Engineering. 120, 115565. DOI: https://doi.org/10.1016/j.jobe.2026.115565

[22] Li, L., Liu, Q., Dao, D., et al., 2023. Dimensional change of cement paste subjected to carbonation in CO_2 sequestration and utilization context: A critical review on the mechanisms. Journal of CO_2 Utilization. 70, 102444. DOI: https://doi.org/10.1016/j.jcou.2023.102444

[23] Wang, L., Lu, X., 2024. A review of the influence of aluminum phases from cement, SCMs and external aluminum phases on the thaumasite sulfate attack in cement-based materials. Journal of Building Engineering. 94, 109966. DOI: https://doi.org/10.1016/j.jobe.2024.109966

[24] Kashani, A., Hameed, R., Khondoker, M.T.H., et al., 2025. Carbon utilization for low-carbon concrete: Prospects for carbonated steel slag and recycled concrete. Resources, Conservation and Recycling. 226, 108698. DOI: https://doi.org/10.1016/j.resconrec.2025.108698

[25] Zhao, C., Zhang, W., Zhang, J., 2026. Degradation mechanisms of cement-based materials exposed to mining wastewater and strategies for improvement via typical SCMs. Journal of Building Engineering. 117, 114883. DOI: https://doi.org/10.1016/j.jobe.2025.114883

[26] Chen, J., Jia, J., Qi, Z., et al., 2026. Impact of synthetic C-S-H-GO seeds on hydration kinetics and pore structure evolution of cement pastes. Cement and Concrete Composites. 168, 106470. DOI: https://doi.org/10.1016/j.cemconcomp.2026.106470

[27] Guo, A., Geng, Y., Ma, H., et al., 2026. Hydration kinetics and mechanism of cement pastes with PEGylated cellulose nanocrystals. Construction and Building

Materials. 508, 145130. DOI: https://doi.org/10.1016/j.conbuildmat.2026.145130

[28] Hirsch, T., Matschei, T., Stephan, D., 2023. The hydration of tricalcium aluminate ($Ca_3Al_2O_6$) in Portland cement-related systems: A review. Cement and Concrete Research. 168, 107150. DOI: https://doi.org/10.1016/j.cemconres.2023.107150

[29] Bisciotti, A., Castellini, S., Neri, A., et al., 2026. Under-calcination thermal reactivation of hydrated cement pastes and construction and demolition waste: A comparison of different commercial products. Case Studies in Construction Materials. 24, e05978. DOI: https://doi.org/10.1016/j.cscm.2026.e05978

[30] Hu, L., Jia, Y., Chen, Z., et al., 2022. An insight of carbonation-hydration kinetics and microstructure characterization of cement paste under accelerated carbonation at early age. Cement and Concrete Composites. 134, 104763. DOI: https://doi.org/10.1016/j.cemconcomp.2022.104763

[31] Peng, L., Jiang, Y., Ban, J., et al., 2023. Mechanism underlying early hydration kinetics of carbonated recycled concrete fines–ordinary Portland cement (CRCF–OPC) paste. Cement and Concrete Composites. 144, 105275. DOI: https://doi.org/10.1016/j.cemconcomp.2023.105275

[32] Al Kindi, H., Abdel-Gawwad, H.A., Meddah, M.S., et al., 2024. An overview of the critical influential parameters on the performance of limestone calcined clay cement paste, mortar, and concrete. Construction and Building Materials. 444, 137615. DOI: https://doi.org/10.1016/j.conbuildmat.2024.137615

[33] Han, K., Guo, T., Shu, X., et al., 2024. Structural build-up of cement pastes—Underlying mechanisms considering the particle packing, colloidal interactions and hydration kinetics. Construction and Building Materials. 438, 137030. DOI: https://doi.org/10.1016/j.conbuildmat.2024.137030

[34] Lothenbach, B., Winnefeld, F., 2006. Thermodynamic modelling of the hydration of Portland cement. Cement and Concrete Research. 36(2), 209–226. DOI: https://doi.org/10.1016/j.cemconres.2005.03.001

[35] Li, K., Yao, J., Hua, S., et al., 2026. Divergent reaction paths in high-Ca/Si alkali-activated backfill: Reconstitutive activation of silica-rich vs. incremental optimization of calcium-rich tailings. Construction and Building Materials. 521, 146082. DOI: https://doi.org/10.1016/j.conbuildmat.2026.146082

[36] Wang, H., Liu, X., Wang, C., et al., 2025. Contributions of ettringite, C-S-H, and free water to shotcrete's mechanical properties: Implications from equivalent cement pastes. Cement and Concrete Research. 196, 107927. DOI: https://doi.org/10.1016/j.cemconres.2025.107927

[37] Ji, X., Liu, Q., Li, Q., et al., 2026. Ca/Si ratio–dependent lubrication mechanisms in calcium silicate hydrate: Implications for concrete fluidity. Journal of Building Engineering. 120, 115240. DOI: https://doi.org/10.1016/j.jobe.2026.115240

[38] Ben Haha, M., Termkhajornkit, P., Ouzia, A., et al., 2023. Low clinker systems—Towards a rational use of SCMs for optimal performance. Cement and Concrete Research. 174, 107312. DOI: https://doi.org/10.1016/j.cemconres.2023.107312

[39] Bullerjahn, M., Zajac, J., Pekarkova, J., et al., 2020. Novel SCM produced by the co-calcination of aluminosilicates with dolomite. Cement and Concrete Research. 134, 106083. DOI: https://doi.org/10.1016/j.cemconres.2020.106083

[40] Bosco, F., Londono-Zuluaga, D., Kruspan, P., et al., 2025. Phase assemblage and microstructure of burnt oil shale-containing blended cements. Cement. 20, 100139. DOI: https://doi.org/10.1016/j.cement.2025.100139

[41] Kim, M.O., Lee, M.K., 2023. Strength and Microstructural Changes in Cementitious Composites Containing Waste Oyster Shell Powder. Buildings. 13(12), 3078. DOI: https://doi.org/10.3390/buildings13123078

[42] Hamada, H.M., Al-Attar, A., Askar, M.K., et al., 2025. Recycled seashells as sustainable aggregates in concrete: Advancing waste management and enhancing performance: A comprehensive review. Journal of Building Engineering. 110, 113067. DOI: https://doi.org/10.1016/j.jobe.2025.113067

[43] Mohamed, D.K.B., Chin, H.Z., Wang, C., et al., 2025. Formation of calcium carbonate polymorphs from ammonium carbonate solutions for aqueous phase CO_2 mineralization of calcium oxide. Journal of Environmental Chemical Engineering. 13(6), 120253. DOI: https://doi.org/10.1016/j.jece.2025.120253

[44] Lee, E., Jia, Z., Yang, T., et al., 2022. Multiscale mechanical design of the lightweight, stiff, and damage-tolerant cuttlebone: A computational study. Acta Biomaterialia. 154, 312–323. DOI: https://doi.org/10.1016/j.actbio.2022.09.057

[45] Mirzabagheri, S., Derhamjani, G., Maharati, S., et al., 2019. Using cuttlebone powder to produce green concrete. Journal of Applied Engineering Sciences. 8(2), 25–28. DOI: https://doi.org/10.2478/jaes-2018-0014

[46] Jiang, J., Tian, Y., Lu, X., et al., 2025. Multiscale investigation of hydration and hardening mechanism in cementitious composite containing CO_2-activation re-

cycled cement paste powder with aragonite whiskers. Journal of Building Engineering. 112, 113888. DOI: https://doi.org/10.1016/j.jobe.2025.113888

[47] Li, Y., Mi, T., Liu, W., et al., 2021. Chemical and mineralogical characteristics of carbonated and uncarbonated cement pastes subjected to high temperatures. Composites Part B: Engineering. 216, 108861. DOI: https://doi.org/10.1016/j.compositesb.2021.108861

[48] Shah, H.A., Meng, W., 2025. Improving the mechanical properties of cement paste with carbonated blast furnace slag by tailoring $CaCO_3$ polymorphs and increasing carbonation degree. Cement and Concrete Composites. 165, 106343. DOI: https://doi.org/10.1016/j.cemconcomp.2025.106343

[49] Li, L., Cao, M., Yin, H., 2019. Comparative roles between aragonite and calcite calcium carbonate whiskers in the hydration and strength of cement paste. Cement and Concrete Composites. 104, 103350. DOI: https://doi.org/10.1016/j.cemconcomp.2019.103350

[50] Hargis, C.W., Chen, I., Wang, Y., et al., 2024. Microstructure development of calcium carbonate cement through polymorphic transformations. Cement and Concrete Composites. 153, 105715. DOI: https://doi.org/10.1016/j.cemconcomp.2024.105715

[51] Hadjadj, M., Guendouz, M., Boukhelkhal, D., 2024. The effect of using seashells as cementitious bio-material and granite industrial waste as fine aggregate on mechanical and durability properties of green flowable sand concrete. Journal of Building Engineering. 87, 108968. DOI: https://doi.org/10.1016/j.jobe.2024.108968

[52] Hay, R., Peng, B., Celik, K., 2023. Filler effects of $CaCO_3$ polymorphs derived from limestone and seashell on hydration and carbonation of reactive magnesium oxide (MgO) cement (RMC). Cement and Concrete Research. 164, 107040. DOI: https://doi.org/10.1016/j.cemconres.2022.107040

[53] Richardson, I.G., 1999. The nature of C-S-H in hardened cements. Cement and Concrete Research. 29(8), 1131–1147. DOI: https://doi.org/10.1016/S0008-8846(99)00168-4

[54] Singh, L.P., Zhu, W., Howind, T., et al., 2017. Quantification and characterization of C-S-H in silica nanoparticles incorporated cementitious system. Cement and Concrete Composites. 79, 106–116. DOI: https://doi.org/10.1016/j.cemconcomp.2017.02.004

[55] Kasaniya, M., Thomas, M.D.A., Moffatt, T., et al., 2024. Microstructure and microanalysis of portland cement pastes with high w/c ratios. Cement and Concrete Research. 183, 107575. DOI: https://doi.org/10.1016/j.cemconres.2024.107575

[56] Diamond, S., 2004. The microstructure of cement paste and concrete—A visual primer. Cement and Concrete Composites. 26(8), 919–933. DOI: https://doi.org/10.1016/j.cemconcomp.2004.02.028

[57] ASTM C150/C150M-24. 2024. Standard Specification for Portland Cement. DOI: https://doi.org/10.1520/C0150_C0150M-24

[58] ASTM E11-24. 2024. Standard Specification for Woven Wire Test Sieve Cloth and Test Sieves. DOI: https://doi.org/10.1520/E0011-24

[59] ASTM C305-20. 2020. Standard Practice for Mechanical Mixing of Hydraulic Cement Pastes and Mortars of Plastic Consistency. DOI: https://doi.org/10.1520/C0305-20

[60] ASTM C109/C109M-20. 2020. Standard Test Method for Compressive Strength of Hydraulic Cement Mortars (Using 2-in. or [50-mm] Cube Specimens). DOI: https://doi.org/10.1520/C0109_C0109M-20

[61] ASTM C511-21. 2021. Standard Specification for Mixing Rooms, Moist Cabinets, Moist Rooms, and Water Storage Tanks Used in the Testing of Hydraulic Cements and Concretes. DOI: https://doi.org/10.1520/C0511-21